Reassessment of shortwave surface cloud radiative forcing in the Arctic: Consideration of surface albedo – cloud interactions

Johannes Stapf[1], André Ehrlich[1], Evelyn Jäkel[1], Christof Lüpkes[2], and Manfred Wendisch[1]

[1]Leipzig Institute for Meteorology (LIM), University of Leipzig, Germany
[2]Alfred Wegener Institute for Polar and Marine Research, Bremerhaven, Germany

Correspondence: Johannes Stapf (johannes.stapf@uni-leipzig.de)

Abstract. The concept of cloud radiative forcing (CRF) is commonly applied to quantify the impact of clouds on the surface radiative energy budget (REB). In the Arctic, radiative interactions between microphysical and macrophysical properties of clouds and the surface modify the warming or cooling effect of clouds, complicating the estimate of CRF obtained from observations or models. Clouds tend to increase the broadband surface albedo over snow surfaces, compared to cloud-free conditions. However, this effect is not adequately represented in the derivation of CRF in the Arctic so far. Therefore, in this study we quantify the effects caused by surface albedo-cloud interactions on the CRF using radiative transfer simulations and below-cloud airborne observations in the heterogeneous springtime marginal sea ice zone (MIZ) during the Arctic CLoud Observations Using airborne measurements during polar Day (ACLOUD) campaign. The impact of a modified surface albedo in the presence of clouds, as compared to cloud-free conditions, and its dependence on cloud optical thickness is found to be relevant for the estimation of the shortwave CRF. A method to consider this surface albedo effect by continuously retrieving the cloud-free surface albedo from observations under cloudy conditions is proposed, using an available snow and ice albedo parameterization. Applying ACLOUD data it is shown that the estimated average shortwave cooling effect by clouds almost doubles over snow and ice covered surfaces (-62 $\mathrm{W\,m^{-2}}$ instead of -32 $\mathrm{W\,m^{-2}}$), if surface albedo-cloud interactions are considered. Concerning the seasonal cycle of the surface albedo it is demonstrated that this effect enhances shortwave cooling in periods where snow dominates the surface, and potentially weakens the cooling by optical thin clouds during the summertime melting season. These findings suggest that the surface albedo-cloud interaction should be considered in global climate models and in long-term studies to obtain a realistic estimate of the shortwave CRF in order to quantify the role of clouds in Arctic amplification.

1 Introduction

Interdisciplinary research conducted within the last decades has led to a broader, but not yet complete understanding of the rapid and, compared to mid-latitudes, enhanced warming in the Arctic (so-called Arctic amplification) (Gillett et al., 2008; Overland et al., 2011; Serreze and Barry, 2011; Stroeve et al., 2012; Jeffries et al., 2013; Cohen et al., 2014; Wendisch et al., 2017). Since the numerous interactions of physical processes, responsible for Arctic amplification, are intertwined and difficult to observe, climate models are needed to quantify the individual contributions of feedback processes to Arctic climate change

(Screens and Simmonds, 2010; Pithan and Mauritsen, 2014). However, the model results show a large spread in representing the feedback mechanisms. One prominent example is the cloud radiative feedback, which includes the effects of an increasing cloud amount in the Arctic, balancing between the potential increase of both longwave downward radiation (positive) and cloud top reflectivity (negative). To enable reliable projections of future climate changes in the Arctic, the understanding of the individual physical processes and feedback mechanisms causing Arctic amplification is required (Pithan and Mauritsen, 2014; Goosse et al., 2018), as well as observations of how clouds influence the Arctic surface radiative energy budget (REB).

To quantify the radiative effect of clouds on the REB, the concept of cloud radiative forcing (CRF, expressed as ΔF) is defined as the difference between the net radiative energy flux densities,

$$F_{\mathrm{net}} = F^{\downarrow} - F^{\uparrow}, \tag{1}$$

also called irradiances, in all-sky conditions ($F_{\mathrm{net,all}}$) and cloud-free ($F_{\mathrm{net,cf}}$) conditions (Ramanathan et al., 1989):

$$\Delta F = F_{\mathrm{net,all}} - F_{\mathrm{net,cf}}. \tag{2}$$

A warming effect at the surface will be caused by clouds if the net radiative flux densities in a cloudy atmosphere are larger than in corresponding cloud-free conditions.

Long-term ground-based observations of CRF in the Arctic (Walsh and Chapman, 1998; Shupe and Intrieri, 2004; Dong et al., 2010; Miller et al., 2015) showed that in the longwave wavelength range clouds tend to warm the surface. The magnitude of the warming is influenced by macrophysical and microphysical cloud properties (e.g., Shupe and Intrieri, 2004) and by regional characteristics (Miller et al., 2015) and climate change (Cox et al., 2015). In the solar spectral range, clouds rather cool, whereby the strength and timing over the year is determined, besides cloud microphysical properties, by the solar zenith angle (SZA) and the seasonal cycle of surface albedo (e.g., Intrieri et al., 2002; Dong et al., 2010; Miller et al., 2015). However, the required cloud-free reference ($F_{\mathrm{net,cf}}$) poses a serious problem to all observations in the cloudy Arctic (Shupe et al., 2011), as the unknown thermodynamic and surface albedo conditions in cloud-free environments is modified by the presence of clouds itself.

Low-level clouds in the Arctic boundary layer cause elevated temperature inversions, modified thermodynamic profiles, and changed turbulent energy and momentum fluxes, as compared to a cloud-free atmosphere. In addition, the clouds modify the surface energy budget by the two competing effects of longwave warming and shortwave cooling, with consequences for the surface temperature and turbulent fluxes. This results in two typical states of thermodynamic profiles (Tjernström and Graversen, 2009) and longwave radiative irradiances (Stramler et al., 2011; Wendisch et al., 2019) observed in the Arctic winter. As demonstrated by Walsh and Chapman (1998), the surface temperature change accompanied by the transitions from cloudy to clear skies is not an instantaneous effect; it rather occurs in the range of hours to days and potentially only advanced boundary layer models might be able to predict the transition between the two states after a given time.

Besides temperature and humidity changes, clouds modify the illumination and reflection of the surface. For highly reflecting snow surfaces, radiative transfer simulations show that two processes are crucial: (i) A cloud-induced weighting of the transmitted downward irradiance to smaller wavelengths, causing an increase of shortwave surface albedo, and (ii) a shift from

mainly direct to rather diffuse irradiance in cloudy conditions, which decreases the shortwave albedo (Warren, 1982). Observations have shown that, in general, there is a tendency that the surface albedo is larger in cloudy, compared to cloud-free conditions (e.g., Grenfell and Perovich, 2008), and was demonstrated for a seasonal cycle by Walsh and Chapman (1998) for highly reflecting surface types. Radiative transfer simulations open up the possibility to tackle the processes involved in the cloud-related surface albedo changes. Both processes (i and ii), have been parameterized for snow and ice, for example by Gardner and Sharp (2010) based on simulations. However, their impact on estimates of CRF in the Arctic have not yet been evaluated.

For this purpose we deploy combined snow surface albedo model and atmospheric radiative transfer simulations and illustrative low-level (below cloud) airborne observations of the REB in the marginal sea ice zone (MIZ) during the Arctic CLoud Observations Using airborne measurements during polar Day (ACLOUD) campaign (Wendisch et al., 2019). After an introduction of the airborne observations, the instrumentation and the radiative transfer simulations (section 2), available approaches to derive the CRF are reviewed in section 3. Furthermore, in this section the interaction between spectral surface albedo and cloud optical thickness and its importance for the estimate of shortwave CRF is analyzed and quantified. In section 4 a method is introduced to retrieve the shortwave surface albedo in the hypothetical cloud-free atmosphere from measurements under cloudy conditions, by using an available snow and ice albedo parameterization from Gardner and Sharp (2010) and a shortwave transmissivity-based retrieval of cloud liquid water path (Appendix A). An application of this approach to ACLOUD airborne observations is presented, extending available REB and CRF datasets/observations in the Arctic including horizontal variability in the heterogeneous MIZ.

2 Observation and modelling

2.1 Airborne measurements

The cloudy atmospheric boundary layer in the MIZ north west of Svalbard was studied using the research aircraft Polar 5 and Polar 6 from the Alfred-Wegener Institute (AWI) during the ACLOUD campaign performed in spring between 23 May and 26 June 2017 (Wendisch et al., 2019). Part of the flights were dedicated to characterize the near-surface radiative energy budget below ABL clouds. From all flights, 16 hours of data measured below an altitude of 250 m (average 80 m) covering a distance of 3700 km are investigated in this paper. The sea ice concentration observed along the low-level flights by instruments mounted on the aircraft is displayed in Fig. 1, together with a Moderate Resolution Imaging Spectroradiometer (MODIS) satellite image showing the sea ice distribution representative for the campaign. During the ACLOUD period, the location of the MIZ, indicated by the contour lines of average sea ice fraction (I_f), was almost stationary (Knudsen et al., 2018). The sea ice was more compact (higher concentration) north of 81° N geographic latitude, and rather heterogeneous towards the west and the open ocean. The majority of flights (66 %) were over sea ice ($I_\mathrm{f} > 80\,\%$), leaving about 17 % over the MIZ as well as 17 % over open ocean ($I_\mathrm{f} < 15\,\%$). As the dataset is merged from different flights covering about six weeks of measurements, it comprises various sea ice characteristics and synoptic situations (Knudsen et al., 2018). However, the data set is still limited and should be considered as a snapshot of the late spring conditions in this region.

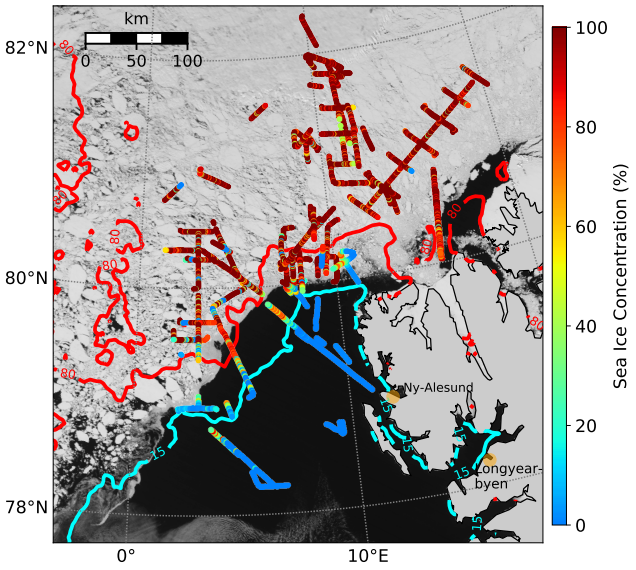

Figure 1. MODIS satellite image on 1 June 2017, representing the typical sea ice distribution during the ACLOUD campaign. All low-level flight sections during the ACLOUD campaign are indicated with the sea ice fraction derived from airborne observations. Red (80 %) and light-blue (15 %) contours indicate the campaign average sea ice fraction from daily sea ice data (Spreen et al., 2008).

2.2 Instrumental payload

The comprehensive instrumentation of Polar 5 and Polar 6 during the ACLOUD campaign is described by Wendisch et al. (2019) and by Ehrlich et al. (2019b). In this paper, shortwave and longwave, upward and downward broadband irradiance have been analyzed from measurements with a frequency of 20 Hz obtained from two sets of Pyranometer (0.2-3.6 µm) and Pyrgeometer (4.5-42 µm). From these irradiance data the net irradiance and surface albedo have been derived. The processing of the Pyranometer and Pyrgeometer data (Stapf et al., 2019), which were used to derive the REB from ACLOUD observations, is detailed in Ehrlich et al. (2019b). Surface brightness temperature was obtain by a Kelvin Infrared Radiation Thermometer (KT–19) (Stapf et al., 2019). The ice fraction I_f along the flight track was estimated from measurements of a digital camera equipped with a hemispheric lens. The geometrically calibrated images were obtained with a sampling frequency of 6 s; from the images the cosine-weighted sea ice concentration was calculated (Jäkel et al., 2019). The local atmospheric thermodynamic state, including air temperature and relative humidity, was determined by dropsondes (Ehrlich et al., 2019a) and aircraft in situ observations (Hartmann et al., 2019) during ascents and descents in the vicinity of the low-level flight sections.

2.3 Radiative transfer simulations

The radiative transfer simulations for the cloud-free conditions were performed with the libRadtran package (Emde et al., 2016) using the one-dimensional, plane-parallel discrete ordinate radiative transfer solver DISORT (Stamnes et al., 1988) and

the molecular absorption parameterization from Kato et al. (1999) for the shortwave spectral range (0.28–4 µm), and from Gasteiger et al. (2014) for the longwave wavelengths range (4–100 µm). The aerosol particle optical thickness was neglected in the simulations, because the full column aerosol information were not available for low-level flights in cloudy conditions. Therefore, the estimated CRF needs to be considered as direct aerosol plus cloud radiative forcing.

The atmospheric state, required as input for the radiative transfer simulations to derive the CRF, was based on radiosoundings performed in Ny-Ålesund (Svalbard) (Maturilli, 2017a, b) and onboard Polarstern (Schmithüsen, 2017), which were partly spatially and temporally separated from the airborne observations by several hundred kilometres and up to three hours. Hence, profiles from in situ measurements of temperature and relative humidity on board of both aircraft and, if available, dropsonde measurements from the Polar 5 aircraft were used to replace the radiosounding layers by the local atmospheric profiles. The atmospheric levels below flight altitude were linearly interpolated to the surface temperature observed by the KT-19 assuming an emissivity of unity. The assumption of the black-body emissivity is justified by the high spectral emissivity for nadir observations in this wavelength range (Hori et al., 2006). The sub-Arctic summer profile (Anderson et al., 1986) was used to complete the profiles including gas concentrations up to 120 km altitude. Daily ozone concentrations in the flight region of ACLOUD were considered and obtained from http://exp-studies.tor.ec.gc.ca/cgi-bin/selectMap. The high vertical resolution of the in situ observations was reduced for the radiative transfer simulations to 30 m below 1000 m and stepwise increases to 5 km at 120 km altitude. The surface albedo was obtained from upward and downward looking pyranometers and a method described in section 4.

Spectral surface albedo values for the sensitivity study in section 3.5 were simulated using the spectral Two-streAm Radiative TransfEr in Snow model (TARTES) (Libois et al., 2013). 3D radiative transfer simulations for the albedo smoothing kernels applied in section 3.4 and the appendix A were performed with the open-source Monte Carlo Atmospheric Radiative Transfer Simulator (MCARaTS) (Iwabuchi, 2006; Iwabuchi and Kobayashi, 2008).

3 Estimate of surface cloud radiative forcing

3.1 Common approaches

To derive the CRF from ground-based observations, simultaneous measurements of net irradiances in cloudy and cloud-free conditions would be needed. From a practical point of view it is impossible to simultaneously measure in cloudy and in cloud-free conditions at the same location. Therefore, the common approach is to measure net irradiances in cloudy conditions, and estimate the respective net irradiances in the hypothetical cloud-free atmosphere. For ground-based observations, two general approaches have been realised to estimate the $F_{\mathrm{net,cf}}$.

Firstly, a radiative transfer based approach, which aims to estimate the instantaneous CRF by simply removing in the simulations the cloud from the observed atmosphere, neglecting changes of the thermodynamic state over time or differences of the cloudy and cloud-free surface albedo (Intrieri et al., 2002; Shupe and Intrieri, 2004; Sedlar et al., 2011; Cox et al., 2015; Wang et al., 2018) and partly Miller et al. (2015) (using cloud-free albedo observations). A second, more climatological approach (Walsh and Chapman, 1998; Dong et al., 2010; Cox et al., 2016) uses observations in cloud-free conditions to extrapolate the

cloud-free state during cloudy periods. In this technique, fitting algorithms from Long and Ackerman (2000) and Long and Turner (2008) are applied, or observed cloud-free/cloudy irradiances are averaged to represent monthly values (Walsh and Chapman, 1998) and partly Dong et al. (2010) (averaging upward longwave irradiance). The cloud-free, shortwave upward irradiance can be obtained from methods described in Long (2005).

In all these methods the physical processes involved in the estimate of $F_{\mathrm{net,cf}}$ are represented differently, resulting in systematic differences in the derived CRF of the individual approaches. From autumn to spring, the longwave CRF derived from the radiative transfer based approach should tend to produce a more positive (warming) CRF compared to the climatological approach. This is due to the in general colder cloud-free surface temperatures, the presence of surface-based and dissipation of elevated temperature inversions in cloud-free conditions. In spring and summer, the surface temperature difference between cloud-free and cloudy state is smaller (Walsh and Chapman, 1998). Therefore, the difference in the CRF estimate between the climatological and radiative transfer based approach will depend on the prevailing conditions controlled by a neutral or potentially even cooling CRF.

The shortwave CRF is strongly affected by the assumed surface albedo. The typically lower values of surface albedo in the cloud-free state (Walsh and Chapman, 1998) should result in more positive shortwave $F_{\mathrm{net,cf}}$, and thus, an increase of the cooling effect of clouds retrieved from the climatological approach relative to the instantaneous radiative transfer based CRF, where a percent deviation of albedo can be related to the deviation of shortwave $F_{\mathrm{net,cf}}$. For the instantaneous CRF, changes in surface albedo between cloudy and cloud-free state have been neglected so far by the use of the observed albedo in the radiative transfer simulations (Intrieri et al., 2002; Shupe and Intrieri, 2004; Sedlar et al., 2011; Wang et al., 2018). Miller et al. (2015) used cloud-free observations of surface albedo fitted linearly as a function of SZA to obtain cloud-free albedo values during cloudy periods. This approach neglects the non-linear dependence of the albedo with SZA (Gardner and Sharp, 2010), the impact of snow grain size and potential seasonal changes of cloud-free surface albedo indicated by the observed albedo shown in Miller et al. (2018), and thus, induces large uncertainties in the estimate of cloud-free shortwave net irradiance and may even distort the obtained seasonal cycle of CRF. The climatological approach from Long (2005) tries to estimate the cloud-free surface albedo during cloudy periods based on cloud-free observations, taking the prevailing SZA into account. However, it should be noted that for longer cloudy periods the cloudy-sky (observed) albedo is used in combination with downward cloud-free irradiance to represent the upward shortwave irradiance, because an extrapolation in changing albedo conditions caused by precipitation and melting events (changes in snow microphysical properties) is not possible. An application of the climatological approach is primarily limited by the high cloud fraction commonly observed in the Arctic (Shupe et al., 2011). It causes large uncertainties in the estimated cloud-free irradiance, as reported by Intrieri et al. (2002), preventing an application to long-term observations with reported high cloud fractions (e.g., Sedlar et al., 2011). Although the climatological approach will produce a more realistic estimate of CRF (especially longwave) with reduced uncertainties and representation of humidity changes (Dong et al., 2006), it remains unclear how representative a monthly average of cloud-free irradiance with a monthly averaged cloud fractions often well above 90 % can be.

By comparing the available studies, using different approaches to estimate the CRF, it becomes evident that the variety of

strategies and the handling of physical processes involved in the CRF in the Arctic limits the comparability of the individual studies and our understanding of CRF in the Arctic.

3.2 Definitions

In this study, we aim to derive the radiative transfer based instantaneous CRF. However, we provide reasons and a solution for the derivation of shortwave CRF using a continuous estimate of the cloud-free surface albedo of snow and ice obtained from observations in cloudy conditions.

To assign processes related to single components of the surface CRF, Eq. 2 is separated in longwave and shortwave terms. The longwave term reads:

$$\Delta F_{\mathrm{lw}} = \left(F^{\downarrow}_{\mathrm{lw,all}} - F^{\uparrow}_{\mathrm{lw,all}}\right) - \left(F^{\downarrow}_{\mathrm{lw,cf}} - F^{\uparrow}_{\mathrm{lw,cf}}\right). \tag{3}$$

As was stated by Cox et al. (2015) the CRF definition refers to net irradiances, while the cloud radiative effect (CRE) characterizes only changes in the downward irradiance. By splitting the upward terms in a component emitted by the surface with a temperature T_{s} and broadband surface emissivity ϵ_{s} of 0.99 (Warren, 1982) as well as a reflected residual of $F^{\downarrow}_{\mathrm{t}}$, the upward term:

$$-F^{\uparrow}_{\mathrm{lw,all}} + F^{\uparrow}_{\mathrm{lw,cf}} = -\epsilon_{\mathrm{s}} \cdot \sigma \cdot T_{\mathrm{s}}^4 - (1-\epsilon_{\mathrm{s}}) \cdot F^{\downarrow}_{\mathrm{lw,all}} + \epsilon_{\mathrm{s}} \cdot \sigma \cdot T_{\mathrm{s}}^4 + (1-\epsilon_{\mathrm{s}}) \cdot F^{\downarrow}_{\mathrm{lw,cf}}, \tag{4}$$

reduces to:

$$-F^{\uparrow}_{\mathrm{lw,all}} + F^{\uparrow}_{\mathrm{lw,cf}} = (1-\epsilon_{\mathrm{s}}) \cdot (F^{\downarrow}_{\mathrm{lw,cf}} - F^{\downarrow}_{\mathrm{lw,all}}). \tag{5}$$

This approach assumes a constant surface temperature in cloudy and cloud-free state, and thus, represents the commonly defined instantaneous longwave CRF similar to Shupe and Intrieri (2004); Sedlar et al. (2011); Miller et al. (2015) and should be considered in the interpretation of the CRF values as discussed in the previous section. The essential input for radiative transfer is the atmospheric temperature, the absorber gas profile and aerosol. Hence, the longwave instantaneous CRF is independent on the upward irradiance and reduces to:

$$\Delta F_{\mathrm{lw}} = F^{\downarrow}_{\mathrm{lw,all}} - F^{\downarrow}_{\mathrm{lw,cf}} + (1-\epsilon_{\mathrm{s}}) \cdot (F^{\downarrow}_{\mathrm{lw,cf}} - F^{\downarrow}_{\mathrm{lw,all}}). \tag{6}$$

The shortwave component of the CRF is given by:

$$\Delta F_{\mathrm{sw}} = \left(F^{\downarrow}_{\mathrm{sw,all}} - F^{\uparrow}_{\mathrm{sw,all}}\right) - \left(F^{\downarrow}_{\mathrm{sw,cf}} - F^{\uparrow}_{\mathrm{sw,cf}}\right). \tag{7}$$

The surface albedo α as a ratio of $F^{\uparrow}_{\mathrm{sw}}$ and $F^{\downarrow}_{\mathrm{sw}}$ measured during low-level flights is introduced into Eq. 7, which leads to the instantaneous shortwave CRF definition:

$$\Delta F_{\mathrm{sw}} = \left(F^{\downarrow}_{\mathrm{sw,all}} - \alpha \cdot F^{\downarrow}_{\mathrm{sw,all}}\right) - \left(F^{\downarrow}_{\mathrm{sw,cf}} - \alpha \cdot F^{\downarrow}_{\mathrm{sw,cf}}\right). \tag{8}$$

The downward shortwave irradiance at the surface in cloud-free conditions ($F^{\downarrow}_{\mathrm{sw,cf}}$) is modulated by the atmospheric profile parameters, but also by the surface albedo. For highly reflective surface types like snow the upward irradiance is significantly higher compared to over mostly absorbing surfaces like ocean water. A part of this upward irradiance is scattered back towards the surface (often referred to as multiple scattering), and thus, contributes to the downward irradiance. Consequently the multiple scattering between surface and atmosphere causes an increase of downward irradiance over snow and ice compared to open ocean. Photons reflected from a bright surfaces like an ice flow might scatter back to the surface increasing the downward radiation over dark areas like surrounding ocean water. For airborne observations in the MIZ, characterized by strong variability in surface albedo due to the variable sea ice cover, as well as ground based measurements in heterogeneous terrain, this, often referred to as, horizontal photon transport due to multiple scattering from the surrounding area to the actual point of observation is not negligible for the estimate of $F^{\downarrow}_{\mathrm{sw}}$ (Ricchiazzi and Gautier, 1998; Kreuter et al., 2014).

To address this problem, the downward irradiance for the cloud-free conditions in regions with heterogeneous surface albedo fields needs to be simulated with an areal averaged albedo α_{ar}, also called effective albedo (Weihs et al., 2001; Wendisch et al., 2004). For example, a local surface albedo over a small lead embedded in homogeneous sea ice is not representative for the areal average surface albedo, determining the scattering processes in cloud-free conditions. To illustrate this approach, we modify Eq. 8 to:

$$\Delta F_{\mathrm{sw}} = \left(F^{\downarrow}_{\mathrm{sw,all}} - \alpha \cdot F^{\downarrow}_{\mathrm{sw,all}}\right) - \left(F^{\downarrow}_{\mathrm{sw,cf}}\Big|_{\alpha_{\mathrm{ar}}} - \alpha \cdot F^{\downarrow}_{\mathrm{sw,cf}}\Big|_{\alpha_{\mathrm{ar}}}\right). \tag{9}$$

where $F^{\downarrow}_{\mathrm{sw,cf}}\Big|_{\alpha_{\mathrm{ar}}}$ represents the downward shortwave irradiance at the surface simulated with the areal average albedo in cloud-free conditions.

Besides affecting the $F^{\downarrow}_{\mathrm{sw}}$, the surface albedo α in Eq. 9 changes for different illumination conditions (cloudy, cloud-free) and cloud optical thickness Warren (1982). Thus, to complete the formulation of the shortwave CRF used in this study, the local surface albedo has to be separated in a cloudy albedo (α_{all}) and an albedo, which continuously represents the cloud-free state α_{cf}. As a result Eq. 9 reads:

$$\Delta F_{\mathrm{sw}} = \left(F^{\downarrow}_{\mathrm{sw,all}} - \alpha_{\mathrm{all}} \cdot F^{\downarrow}_{\mathrm{sw,all}}\right) - \left(F^{\downarrow}_{\mathrm{sw,cf}}\Big|_{\alpha_{\mathrm{ar}}} - \alpha_{\mathrm{cf}} \cdot F^{\downarrow}_{\mathrm{sw,cf}}\Big|_{\alpha_{\mathrm{ar}}}\right). \tag{10}$$

In the following sections, these two key components (the impact of horizontal photon transport $F^{\downarrow}_{\mathrm{sw,cf}}\Big|_{\alpha_{\mathrm{ar}}}$ (section 3.4) and the impact of clouds on α_{cf} of the CRF estimate (section 3.5)) are analysed using synthetic radiative transfer simulations and illustrative ACLOUD observations, in order to quantify their separate impact on the CRF in the Arctic.

3.3 Impact of local thermodynamic atmospheric state

In the MIZ, the thermodynamic state of the atmosphere changes within short distances due to the influence of the surface on the airmass (warm air moving north over cold sea ice, cold air moving south over warm open ocean) (e.g., Lampert et al., 2012). As was shown by Tjernström et al. (2015, 2019) such events might significantly impact the local energy budget along the trajectory. As an example of temperature profiles being influence by large scale processes, the spatial variability of air

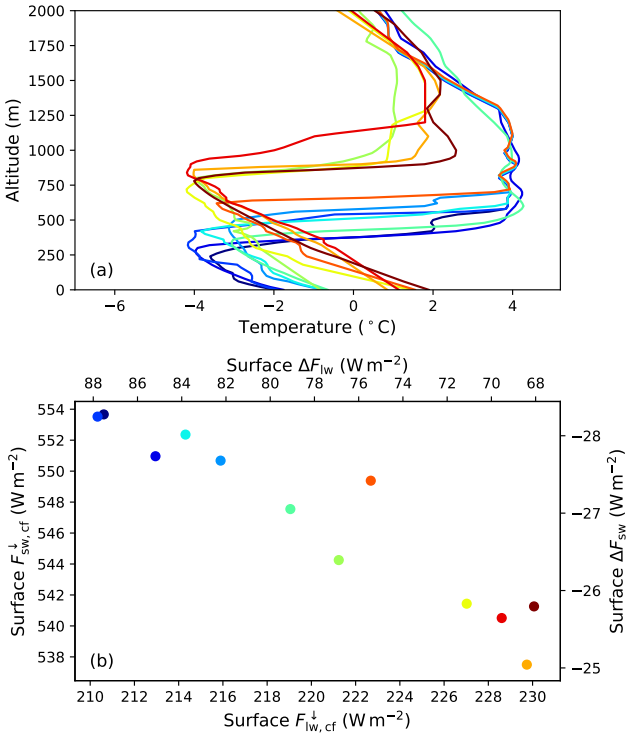

Figure 2. (a) Temperature profiles observed during the warm air intrusion on 2 June 2017. The profiles are obtained from dropsonde and in situ measurements (merged with radiosoundings) and are color-coded by the air temperature in the lowest 200 m. (b) Correlation between simulated cloud-free $F^{\downarrow}_{\mathrm{sw}}$ and $F^{\downarrow}_{\mathrm{lw}}$ assuming the observed atmospheric profiles from (a) (same color code). The second x and y axis shows the expected longwave/shortwave CRF at the surface by assuming a constant $F^{\downarrow}_{\mathrm{sw,all}}$ (412 W m^{-2}) and $F^{\downarrow}_{\mathrm{lw,all}}$ (298 W m^{-2}) based on observations. For a better comparability, the surface albedo and the SZA was fixed in the simulations to 0.8 and 60°, respectively.

temperature profiles measured on 2 June 2017 by the aircraft instruments (Polar 6) and dropsondes is illustrated in Fig. 2a. The synoptical situation during this flight (west of Svalbard) was characterized by warm air advection with optically thick clouds moving from the open ocean over the MIZ. The consecutive in situ profiles illustrate the changes in inversion height along the flight leg, which changed from roughly 800 m over the ocean to 250 m over the sea ice within 50 to 100 km. The relative humidity (not shown here) changed accordingly.

For the shown profiles, radiative transfer simulations are performed to calculate $F^{\downarrow}_{\mathrm{sw,cf}}$ and $F^{\downarrow}_{\mathrm{lw,cf}}$ for the cloud-free reference case. The surface albedo and SZA is fixed for this sensitivity study to 0.8 and 60° respectively, similar to the observed conditions over sea ice during that flight, in order to avoid any effects induced by changing SZA or surface albedo. Fig. 2b shows the simulated downward irradiance and corresponding values of the shortwave and longwave CRF. While longwave irradiance increases with increasing humidity and temperature (enhanced emission), the shortwave irradiance decreases (enhanced scattering and absorption). The CRF for each case is estimated using the average observed $F^{\downarrow}_{\mathrm{sw,all}}$ and $F^{\downarrow}_{\mathrm{lw,all}}$ during the low-level

section on 2 June 2017. The results show a strong variability in ΔF induced by changes in the thermodynamic structure. The relative deviations range up to 29 % for the longwave and 11 % for the shortwave CRF, which highlights that neglecting changes of the atmospheric thermodynamic state within a few kilometers can cause significant errors in the retrieved CRF. Especially for airmass transformation like warm air intrusions and cold air outbreaks in the Arctic (Pithan et al., 2018), this is a relevant issue, and requires a precise representation of airmass transformations by models or local in situ observations along the trajectory.

Another aspect regarding the thermodynamic state of the atmosphere is the impact of the average aircraft flight altitude (here 80 m) on the estimate of CRF. The $F^{\downarrow}_{\mathrm{lw,cf}}$ is simulated for local flight altitude and not exactly for the surface. Due to the fact that the vertical gradient $dF^{\downarrow}_{\mathrm{lw}}/dz$ and $dF^{\uparrow}_{\mathrm{lw}}/dz$ below clouds remains almost the same with or without a cloud in the radiative transfer simulations (for atmospheric profiles as observed during ACLOUD), the observed CRF in flight altitude can be related to surface CRF values causing uncertainties below $\pm 5\,\mathrm{W\,m^{-2}}$. For an interpretation of single longwave irradiance directions and a comparison to surface observations (both not shown in this study), changes due to prevailing near-surface temperature profile have to be expected.

3.4 Impact of areal versus local surface albedo

In Fig. 1 the variability of the observed sea ice fraction I_{f} can directly be related to the variability in the surface albedo distributions in the MIZ and will influence the observed field of downward shortwave irradiance. For the observations carried out on 23 May 2017, the measured broadband surface albedo along the flight track is shown in Fig. 3a. The low-level section started in the MIZ over large ice floes and small leads and ended over the open ocean in vicinity of the ice edge with occasionally scattered sea ice floe fields. Leads with the size of a few tens of meters up to a few kilometers caused a highly variable local surface albedo.

In Fig. 3b the simulated $F^{\downarrow}_{\mathrm{sw,cf}}$ using the observed 20 Hz surface albedo illustrates the problems related with strong albedo fluctuations. The simulated $F^{\downarrow}_{\mathrm{sw,cf}}$ changes on small horizontal scales by up to $35\,\mathrm{W\,m^{-2}}$ (SZA average: 59.2°). However, due to horizontal photon transport from surrounding ice fields, in reality the changes in $F^{\downarrow}_{\mathrm{sw,cf}}$ are less pronounced. The quantitative impact of multiple scattering on $F^{\downarrow}_{\mathrm{sw,cf}}$ is indicated by the gray shaded area in Fig. 3b with a maximum contribution of almost $40\,\mathrm{W\,m^{-2}}$ (relative to open ocean). Therefore, the downward irradiance for the cloud-free conditions, required for Eq. 10, needs to be simulated with an appropriate areal averaged albedo representing the multiple scattering contribution from the surrounding albedo fields.

To estimate a required filter shape and width to obtain an areal averaged albedo, 3D radiative transfer simulations of a typical scenario are performed (not shown here), where leads of different sizes are embedded in homogeneous sea ice similar to the study from Podgorny et al. (2018). The simulated irradiance of the 3D model output in the vicinity of the leads is reproduced by 1D simulations by applying the filter embedded in Fig. 3b to the theoretically observed albedo and by using the obtained areal averaged albedo for the 1D model simulations to continuously estimate the $F^{\downarrow}_{\mathrm{sw,cf}}$. The appropriate weighting of near-field and

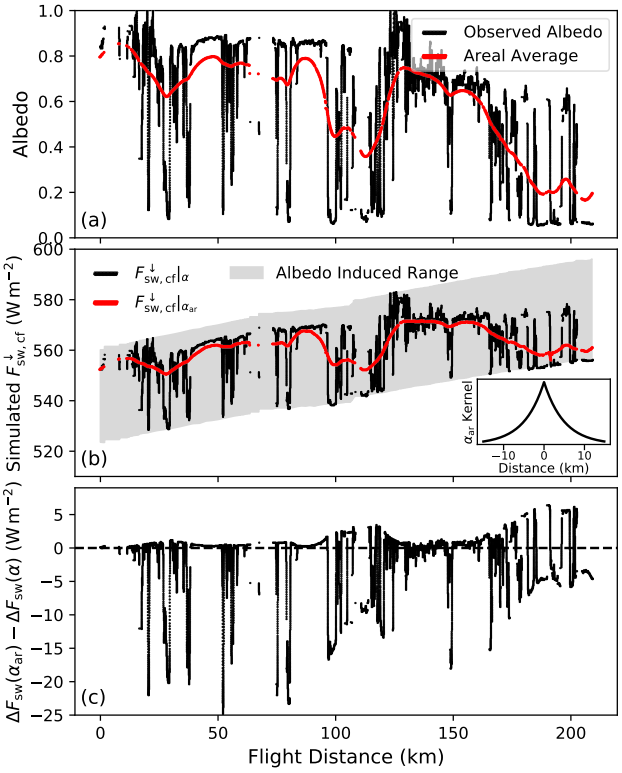

Figure 3. Time series (covered distance) of measured broadband surface albedo (black) (a) and simulated $F^{\downarrow}_{\mathrm{sw,cf}}$ (b) along the low-level flight track during the 23 May 2017. The red line in (a) shows the areal averaged albedo using the kernel embedded in (b). (b) The gray area shows the potential variability of $F^{\downarrow}_{\mathrm{sw,cf}}$ due to surface albedo changes. The black and red scatter shows the $F^{\downarrow}_{\mathrm{sw,cf}}\Big|_{\alpha}$ and $F^{\downarrow}_{\mathrm{sw,cf}}\Big|_{\alpha_{\mathrm{ar}}}$ respectively. (c) Difference in shortwave CRF estimate between $\Delta F_{\mathrm{sw}}(\alpha_{\mathrm{ar}})$ and $\Delta F_{\mathrm{sw}}(\alpha)$.

far-field albedo is applied by kernel k defined by a Laplace-distribution:

$$k(x,\mu,\gamma) = \frac{1}{2\gamma}\left(-\frac{|x-\mu|}{\gamma}\right), \tag{11}$$

with γ of 5 km, the median μ and a scale x of 30 km. This rather large filter width indicates that small leads below 1km embedded in homogeneous sea ice show a minor impact on $F^{\downarrow}_{\mathrm{sw}}$ in cloud-free conditions.

The resulting areal averaged albedo is shown in Fig. 3a, together with the simulated $F^{\downarrow}_{\mathrm{sw,cf}}\Big|_{\alpha_{\mathrm{ar}}}$ (Fig. 3b), which follows the large scale trends of surface albedo but mitigates small scale fluctuations. Neglecting these effects would result in uncertainties of the local shortwave CRF estimate, as shown in Fig. 3c. On average, the effect for flight section in Fig. 3 is of minor importance (average -1.9 $\mathrm{W\,m^{-2}}$), because under- and overestimation of shortwave CRF cancel in this specific example, similar to results from Benner et al. (2001). Nevertheless, on a local scale it should be highlighted that due to horizontal photon transport the $F^{\downarrow}_{\mathrm{sw,cf}}\Big|_{\alpha_{\mathrm{ar}}}$ is up to 28 $\mathrm{W\,m^{-2}}$ larger above leads compared to the $F^{\downarrow}_{\mathrm{sw,cf}}\Big|_{\alpha}$. The difference in the derived CRF reaches values between -25 $\mathrm{W\,m^{-2}}$ over open water embedded in homogeneous sea ice, where the $F^{\downarrow}_{\mathrm{sw,cf}}$ is underestimated by applying

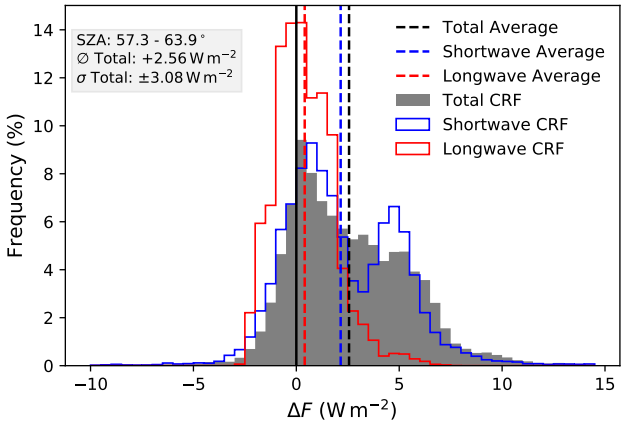

Figure 4. Histogram of shortwave, longwave and total ΔF derived during the cloud-free ACLOUD flight on 25 June 2017. Statistics are given in the gray box (mean ∅, standard deviation σ).

the local albedo, and +6 $\mathrm{W\,m^{-2}}$ above scattered ice floe fields in the ocean with an overestimation of $F^{\downarrow}_{\mathrm{sw,cf}}$. Hence, the uncertainties and artificial fluctuations in CRF are limited by applying the smoothed albedo in the $F^{\downarrow}_{\mathrm{sw,cf}}$ simulations. This enables a more reliable estimate of the CRF in the heterogeneous MIZ and over the specific surface types, taking into account that the complexity of surface albedo fields in the MIZ can only be insufficiently represented by this simplified approach to estimate the areal averaged albedo.

3.4.1 Uncertainty estimate in cloud-free conditions

During ACLOUD a flight in cloud-free conditions on 25 June 2017 can be used for a comparison between measured and simulated irradiances to estimate the accuracy of this dataset. The difference between observed and simulated $F^{\downarrow}_{\mathrm{cf}}$ for the low level flights of both aircraft (2.1 hours of data) is 5.7$\pm$7.1 $\mathrm{W\,m^{-2}}$ (1.1 %) in the shortwave and 0.41$\pm$1.45 $\mathrm{W\,m^{-2}}$ (0.2 %) in the longwave irradiance. The histograms of the CRF for that day are shown in Fig. 4. The mean values of the entire flight section is 2.15 $\mathrm{W\,m^{-2}}$ in the shortwave and 0.41 $\mathrm{W\,m^{-2}}$ in the longwave. The slightly positive CRF might be caused by the upper air sounding approximately 300 km in the south of the flight track or the aerosol conditions (aerosol optical thickness was set to zero in the simulation). In addition to the measurement uncertainties of the used broadband radiometer (<3 %, (Ehrlich et al., 2019b)), the radiative transfer modelling can induce a bias (<2 %) in the shortwave wavelength ranges (Randles et al., 2013). Due to the absence of cloud-free conditions during other low-level flights of the ACLOUD campaign this comparison can be considered as a rough estimate of potential uncertainties during the whole ACLOUD campaign.

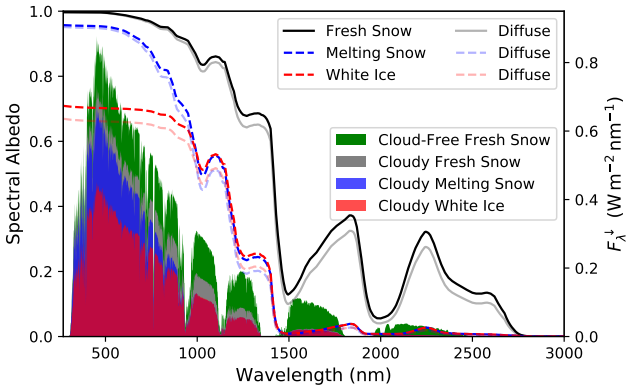

Figure 5. Simulated spectral snow albedo of three seasonal sea ice types for different SSA and snow thickness above sea ice with spectrally neutral albedo of 0.5. Non-attenuated lines show the albedo of the cloud-free situations (SZA of 65°), attenuated lines the albedo for overcast conditions. The downward irradiance (right y-axis) simulated for these cases are shown by the shaded areas. Green shows the cloud-free spectra over fresh snow, gray, blue and red under cloudy conditions (LWP of 80 g m^{-2}) for the surface albedo related by the colors.

3.5 Impact of clouds on the surface albedo

The effect of clouds on the broadband surface albedo, implemented in Eq. 10, is analysed by a set of spectral albedos of three sea ice types common in the Arctic for different seasons. Different snow packs with a density of 300 kg m^{-2} are specified with various values of snow geometric thickness and specific surface area (SSA, a measure of snow grain size) (Gardner and Sharp, 2010), and located above a layer representing bare sea ice with a wavelength constant broadband albedo of 0.5. Fresh cold and dry snow (SSA = 80 m^2 kg^{-1}, 20 cm thick) represents early to late spring conditions, melting snow (SSA = 5 m^2 kg^{-1}, 20 cm thick) the melting season in late spring early summer, and thin melting snow/white ice (SSA = 5 m^2 kg^{-1}, 1 cm thick) summer conditions, before the melt pond formation. The spectral albedo for each type is simulated with the TARTES model for 65° SZA; the respective results are shown in Fig. 5 (solid lines) together with simulated downward irradiances from the atmospheric radiative transfer simulations using libRadtran (shaded spectra).

The general impact of snow properties on the spectral albedo is characterized by stronger absorption at longer wavelengths with decreasing SSA (increasing effective grain size) and can be seen by comparing the albedo of fresh and melting snow in Fig. 5. A decreasing SSA amplifies the contrast between shorter and longer wavelength. A thinning of the snow layer or impurities in snow enhance the absorption mainly in the shorter visible wavelength range, as illustrated by the albedo of melting snow in comparison to that of white ice.

Two processes influencing the broadband snow albedo are related to the transition from cloud-free to cloudy atmospheric conditions. In an overcast atmosphere with clouds of sufficient optical thickness, mainly diffuse radiation illuminates the surface as compared to cloud-free conditions, when the direct shortwave radiation dominates. In the Arctic, large values of SZA ($>$ 50°) are common. In overcast conditions, scattering processes in clouds decrease the averaged incoming (effective) angle of the mainly diffuse irradiance to approximately 50° above snow (Warren, 1982). With decreasing effective SZA, the penetra-

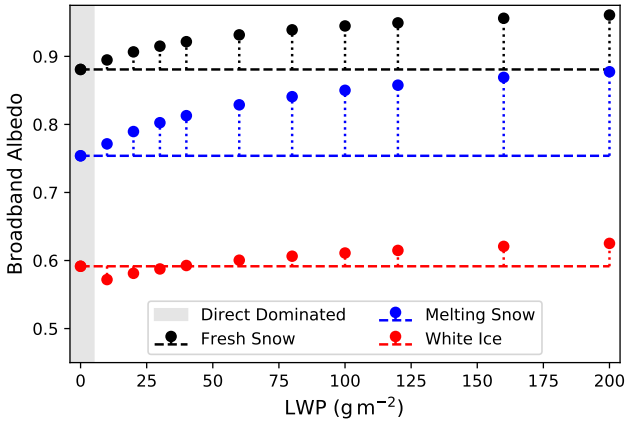

Figure 6. Broadband albedo integrated from simulated up- and downward spectral irradiance as a function of cloud LWP using the color-related spectral albedos of Fig 5. The approximate area of direct dominated/ cloud free radiation is indicated by the gray shading (SZA of 65°). The horizontal line indicates the cloud-free albedo as a reference.

tion depths of photons into the snow and ice surface increases, enhancing the probability of absorption, and thus decrease the overall broadband surface albedo (Warren, 1982). In Fig. 5 this effect is illustrated by the attenuated lines representing the respective diffuse albedo values. Compared to the surface albedo of fresh snow in cloud-free atmospheric conditions (black line) the change of effective SZA (in this example from 65° to approximately 50° SZA) causes a lower spectral surface albedo (attenuated black line) in the non-visible wavelength range, while the highly reflective visible wavelengths are not affected. Thus, for this surface type only a small impact on the actual broadband albedo can be expected, because for the majority of the related downward shortwave irradiance (e.g. grey shaded area in Fig. 5) the albedo remains high. However, for surface types with a spectral albedo characterized by stronger absorption in the visible wavelength range (albedo of white ice, red line in Fig. 5), also stronger changes between direct-dominated and diffuse broadband albedo are expected (attenuated red line).

Besides the changing effective SZA, clouds reduce the incident irradiance by attenuating especially in the near-infrared wavelength range (Grenfell and Perovich, 2008), which can be seen in Fig. 5 by comparing the green and gray shaded spectrum representing cloud-free, cloudy conditions with a liquid water path (LWP) of $80\,\mathrm{g\,m^{-2}}$, respectively. With increasing cloud optical thickness the spectral slope of downward irradiance is imprinted in the surface spectra. As the spectral albedo of ice and snow is higher for shorter wavelengths (e.g. black line in Fig. 5) and the downward irradiance spectra is shifted to shorter wavelength, the wavelength integrated (broadband) albedo will increase. This effect becomes stronger the more pronounced the slope between visible and near-infrared wavelength becomes, which can be induced by two processes: either stronger absorption by clouds due to a higher LWP, or by the underlying surface albedo with decreasing near-infrared albedo. The latter is controlled by decreasing SSA (transition from fresh to melting snow), resulting reduced near-infrared reflection of the surface (compare black and blue lines in Fig. 5), which indirectly affects $F_{\mathrm{sw}}^{\downarrow}$ by reduced multiple scattering between surface and clouds in this wavelength range (compare grey and blue shaded spectra). However, for the spectral albedo of white ice (red

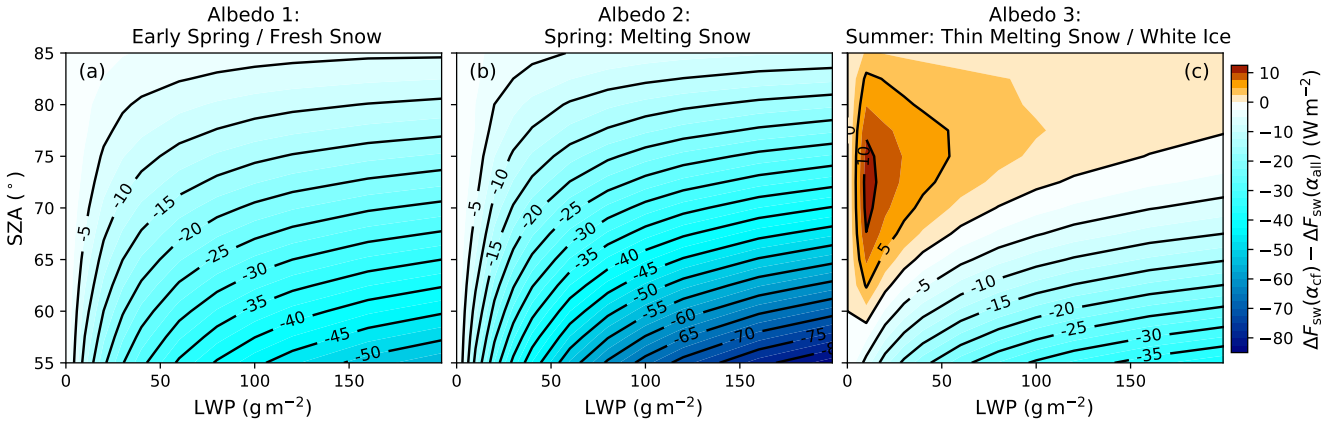

Figure 7. Bias of the shortwave CRF ($\Delta F_{\mathrm{sw}}(\alpha_{\mathrm{cf}}) - \Delta F_{\mathrm{sw}}(\alpha_{\mathrm{all}})$) caused by neglecting the change between observed cloudy and cloud-free surface albedo as a function of cloud LWP and SZA. The three albedo types from Fig. 5 have been assumed, (a) fresh snow representative for early spring, (b) melting snow during late spring, and (c) thin melting snow/white ice found in early summer.

line) the slope in the $F^{\downarrow}_{\mathrm{sw}}$ spectra (red shaded) is less pronounced, and a weaker increase of broadband albedo is expected for increasing LWP.

For all three surface albedo types shown in Fig. 5, the effect of clouds (as a function of LWP) on the broadband surface albedo, is presented in Fig. 6 for a SZA of 65°. An effective cloud droplet radius (r_{eff}) of 8 µm is used. The gray area indicates the direct-dominated radiation in cloud-free conditions; dashed lines represent the cloud-free albedo value as a reference.

For the different surface types a significant change of up to 12 % relative to the individual cloud-free values of albedo can be found with increasing cloud optical thickness, which is modulated by the interaction of surface and cloud radiative properties. In general, the lower the ratio of spectral albedo between shorter and longer wavelengths, the stronger is the increase of broadband albedo with increasing LWP, as shown for the black and blue scatter in Fig. 6 representing fresh and melting snow, respectively. Spectral absorption of the surface in shorter wavelengths strongly decreases the broadband albedo, but it will also alter the behaviour with increasing LWP (Fig. 6, red). For low LWP values, the broadband albedo is lower compared to cloud-free conditions due to a significant lower spectral diffuse albedo (dashed and attenuated dashed red in Fig. 5) at shorter wavelengths. However, with increasing LWP the weighting effect in transmitted $F^{\downarrow}_{\mathrm{sw}}$ to shorter wavelength compensates/dominates and, as a consequence, it increases the broadband surface albedo compared to cloud-free conditions.

3.5.1 Surface albedo-cloud interaction and CRF

In calculations of the instantaneous CRF based on radiative transfer, the observed surface albedo below clouds serves as a reference for the simulations of $F_{\mathrm{net,cf}}$ and calculation of ΔF_{sw}. Also weather and climate models, where the change of the broadband albedo with increasing LWP is not, or only poorly, parameterized, may have a bias in the estimated CRF as well as in the $F_{\mathrm{net,cf}}$ in cloudy conditions. To estimate the significance of the surface albedo-cloud interaction, radiative transfer

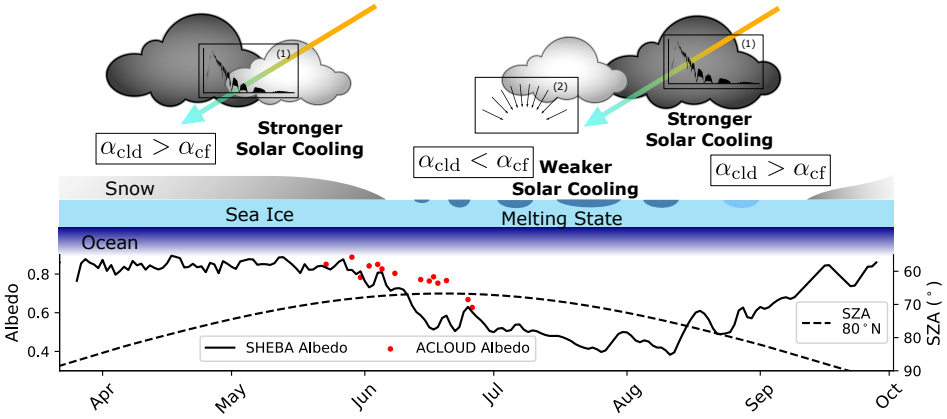

Figure 8. Hypothetical scheme of the seasonal cycle of surface albedo-cloud interaction related modification of shortwave CRF. Dominant processes influencing the transition from cloudy (cld) to cloud-free surface albedo in the specific season are represented by the icons (1) (weighting of downward irradiance to shorter wavelength with increasing LWP) and (2) (transition from direct to diffuse radiative transfer). The seasonal cycle of surface broadband albedo is shown by SHEBA observations (200 m albedo line). Averaged ACLOUD observations for homogeneous sea ice ($I_f > 95\,\%$) are shown in red scatter points. Computed daily averaged SZA for 80° N in dashed black.

simulations are used to calculate the shortwave CRF, either assuming the correct cloud-free albedo as a reference, or the prevailing cloudy albedo, as shown in Fig 6. The difference in CRF $\Delta F_{sw}(\alpha_{cf}) - \Delta F_{sw}(\alpha_{all})$ between both approaches, and thus, an underestimate of the shortwave cooling effect if the cloudy albedo is used, is shown in Fig. 7 as a function of SZA and LWP ($r_{eff} = 8\,\mu m$). Negative (bluish) values indicate a stronger shortwave cooling effect for $\Delta F_{sw}(\alpha_{cf})$. The simulations are performed for all three sea ice types in Fig. 5 and changes in direct/diffuse radiation due to SZA are taken into account.

In case of snow surfaces, influenced by the SSA (Fig. 7a and b), the cooling effect of clouds on the surface is underestimated (blue colors), if the cloudy albedo is used to derive the shortwave CRF. In general, the lower the SZA and the higher the LWP, the stronger the underestimation of the cooling effect becomes. Furthermore, the coarser the snow grains (melting snow) the stronger the underestimation. In contrast, during summer and for thin melting snow or white ice (Fig. 7c), the cooling effect is overestimated for low sun and optically thin clouds, if the apparent cloudy albedo is used for ΔF_{sw}, and shifts towards the underestimation for optically thick clouds and/or lower SZA.

The values of underestimation/overestimation indicate that the surface albedo-cloud interaction significantly impact the estimate of shortwave CRF and the obtained values from the different approaches in the available CRF studies in the Arctic. Especially for clouds over snow, the cooling effect of clouds is considerably larger. Due to the dependence on specific spectral surface albedo types, a seasonal dependence of this surface albedo-cloud interaction, and thus, the shortwave CRF, is indicated.

In Fig. 8 a hypothetical scheme of the modified seasonal cycle of CRF due to the surface albedo-cloud interaction, is proposed. The time series of surface albedo as observed during the Surface Heat Budget of the Arctic Ocean (SHEBA) campaign (Uttal et al., 2002) is shown, to illustrate the seasonal transition as reported by Perovich et al. (2002), together with a daily averaged SZA for 80° N. During spring, early summer and autumn surface albedo values related to snow on sea ice are found. The

results from Fig. 7 indicate that the shift of transmitted irradiance towards shorter wavelength (process 1 in Fig. 8) is dominant in these situations and clouds induce a stronger cooling effect on the surface. With the beginning of the melting season, the change between diffuse and direct albedo will dominate (process 2) for optical thin clouds and high SZA, potentially reducing the cooling effect on the surface in dependence of the conditions. In this period the onset of melting (rapidly decreasing albedo), the melt pond fraction, the SZA (dashed black line in Fig. 8) together with the cloud optical thickness would critically influences the sign of this modification. However, as was reported by Walsh and Chapman (1998), for regions where even in summer snow or bare sea ice is found, all year long a lower albedo in cloud-free conditions, and thus, a stronger cooling effects of clouds can be expected. Though, conclusions about the annual averaged shortwave CRF influence by surface albedo-cloud interactions are not yet possible, as coupled surface-atmosphere radiative transfer models capable of representing surface types like melt ponds are required to study the full seasonal cycle. Also for climate models with simple albedo parameterizations, the results from Fig. 7 can be interpreted as a potential bias in the shortwave F_{net} and CRF depending on the cloud optical thickness.

For the ACLOUD campaign, snow on ice was the dominant surface type (Jäkel et al., 2019), which explains the slightly later decrease in surface albedo (Fig. 8, red scatter points) compared to SHEBA data (black) and represents the transition from cold and fresh snow to melting snow. Transferred to the results from Fig. 7 a stronger cooling effect of the clouds should be expected during ACLOUD.

4 Cloud radiative forcing during ACLOUD

The problems of calculating the CRF, as discussed in sections 3.3, 3.4 and 3.5 are considered in the data processing of the ACLOUD measurements. Therefore, the closest available atmospheric profile is applied in the radiative transfer simulations as well as the areal averaged surface albedo, required for the simulations of $F^{\downarrow}_{\mathrm{sw,cf}}$, are calculated for the low-level flights. The final step is to continuously retrieve the local surface albedo under cloud-free atmospheric conditions from the observed cloudy-sky albedo, in order to obtain a more realistic estimate of the CRF.

4.1 Retrieving the cloud-free albedo from cloudy-sky observations

To obtain an estimate of the cloud-free albedo, the broadband albedo parameterization developed by Gardner and Sharp (2010) for snow and ice surfaces is applied. Gardner and Sharp (2010) considered the dependence of broadband albedo with respect to SZA, SSA, concentration of absorbing carbon, as well as the cloud optical thickness. The parameterization is valid for homogeneous snow and ice including a cloud optical thickness below 30 (LWP of 133 $\mathrm{g\,m^{-2}}$ with r_{eff} = 8 µm). During ACLOUD, the observed albedo ranged between 0.9 for homogeneous sea ice covered with cold snow and values below 0.6 during the later stage of the campaign with the onset of melting (Wendisch et al., 2019; Jäkel et al., 2019). To include these data in the analysis and cover this albedo range only as a function of grain size (SSA), an impurity load of absorbing carbon of 0.1 ppmw is chosen, which causes a similar spectral behaviour of the albedo as changes in snow thickness. As shown by Jäkel et al. (2019), snow overlaying sea ice was the predominant surface type over closed sea ice during ACLOUD. Nevertheless,

the potential variability in the spectral surface albedo with respect to absorption in the short wavelength ranges during the campaign is only roughly covered by this approach and needs to be considered in the interpretation of the obtained cloud-free albedo values.

The parameterization is used to generate lookup tables as a function of observed variables of cloudy-sky albedo, LWP and local SZA. Isolines of SSA are used to extrapolate the cloud-free albedo (LWP = $0\,\mathrm{g\,m^{-2}}$). To apply the albedo parameterization by Gardner and Sharp (2010) the cloud optical thickness or LWP is required. As the cloud properties change on small horizontal scales, a retrieval of LWP based on the airborne measurements of cloud transmissivity was used, which is described in the appendix A.

4.1.1 Application to the observations

The dependence of the surface albedo on the cloud LWP is shown in Fig. 9 as measured over homogeneous sea ice (selected $I_\mathrm{f} > 98\,\%$) on 14 June 2017. In addition, the albedo parameterization by Gardner and Sharp (2010) for the averaged SZA (63.7°) and different values of SSA is shown. During 1.7 hours of low-level flights below clouds, a large area was mapped (80.7-81.8° N,9.8-12.7° E) and a strong variability in optical thickness including occasional openings with direct illumination of the surface and optical thick multilayer clouds was covered. The surface temperatures were close to zero, indicating the beginning melting season (Jäkel et al., 2019). The observed albedo values averaged for $6\,\mathrm{g\,m^{-2}}$ bins (dashed red in Fig. 9) change from 0.7 for low values of LWP to albedo values above 0.8 for a LWP larger than $100\,\mathrm{g\,m^{-2}}$. While the overall trend of increasing albedo with increasing LWP is represented, the slope follows the parameterization for a SSA between $3\,\mathrm{m^2\,kg^{-1}}$ for lower LWP values and $6\,\mathrm{m^2\,kg^{-1}}$ for higher LWP. This might be related to different observed cloud and surface areas as the distribution includes data from both aircraft.

Extrapolating the observations (pair of variates) of LWP equivalent and surface albedo along isolines of SSA to a LWP of zero gives an estimate of the cloud-free surface albedo. For the example given here, for a α_all of 0.82 and LWP of $100\,\mathrm{g\,m^{-2}}$ a cloud-free albedo of 0.74 would be estimated, and thus, 0.06 lower than the observed one in overcast conditions. For LWP values exceeding the limitation of the parameterization the maximum valid LWP was applied. Rarely occurring surface albedo values above/below the range of the parameterization from Gardner and Sharp (2010) have been filtered out.

A comparison of measured (all-sky) α_all and extrapolated cloud-free albedo α_cf is shown in Fig. 10a. The frequency distributions are calculated for all low-level flights during ACLOUD over homogeneous sea ice ($I_\mathrm{f} > 98\,\%$). The broad distribution of observed albedo illustrates the seasonal transition of sea ice properties from a cold period end of May 2017 into the melting season in June 2017 (Wendisch et al., 2019; Jäkel et al., 2019). On average, the cloudy albedo (LWP > $1\,\mathrm{g\,m^{-2}}$) was about 0.8. The estimated cloud-free albedo gives an average value of 0.74, which is approximately 6 % lower than α_all. The distribution of α_cf is slightly narrower than the measured one in cloudy conditions, because the majority of cloud-free flight sections took place close to the end of the campaign with low values of surface albedo, and thus, gives a lower bound to the distribution.

The uncertainties in the estimate α_cf and the shortwave $F_\mathrm{net,cf}$ depend mainly on the observed α_all, as was investigated by applying synthetic albedo and LWP distributions to the lookup tables. Due to the non-linear increase of α_all with LWP, the potential error induced by uncertainties in the retrieved LWP is larger for lower LWP. Additionally, the effect depends on the

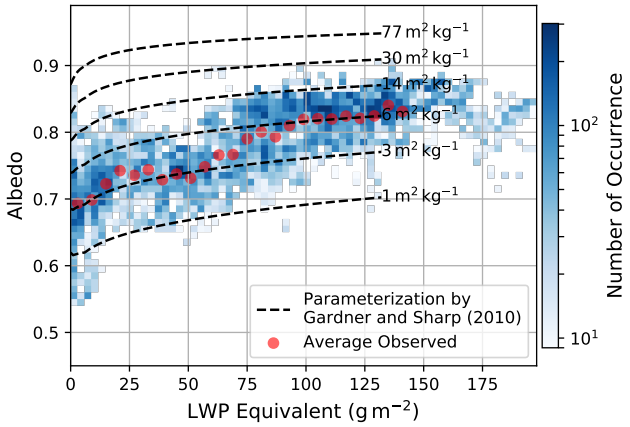

Figure 9. Relation between broadband albedo and retrieved LWP equivalent observed on 14 June 2017 ACLOUD flight over homogeneous sea ice ($I_\mathrm{f} > 98\,\%$). The broadband albedo parameterization by Gardner and Sharp (2010) is shown for different SSA and the average SZA by the dashed lines (impurity load of 0.1ppmw). Averaged observations ($6\,\mathrm{g\,m^{-2}}$ bins) are shown in red scatter.

prevailing surface types. The overall uncertainty in the cloud-free shortwave net irradiances using the retrieved α_cf can be expected to range below 20 % above homogeneous high surface albedos, decreasing with decreasing surface albedo.

Fig. 10a shows only measurements conducted over homogeneous sea ice, which was frequently observed during ACLOUD. In the MIZ, though, the heterogeneous sea ice and the corresponding reduced surface albedo prevents an application of the original parametrization by Gardner and Sharp (2010). However, making use of the cosine weighted sea ice fraction I_f and its linear relation to the albedo, changes due to the surface albedo-cloud interaction can be scaled to the prevailing I_f by assuming diffuse radiative transfer (Lambertian albedo) (not shown in this study).

4.2 Correction of CRF

To illustrate the effect of surface albedo-cloud interactions on the calculation of the CRF during the ACLOUD campaign, the CRF is computed using both measured cloudy albedo (α_all) and the estimated cloud-free albedo (α_cf). Fig. 10b shows the frequency distribution of the shortwave CRF for both solutions, observed over homogeneous sea ice ($I_\mathrm{f} > 98\,\%$). The CRF based on the observed albedo (gray bars) shows a bimodal distribution. The mode around $0\,\mathrm{W\,m^{-2}}$ represents cloud-free situations and heterogeneous optically thin clouds, where 3D effects induced occasionally positive shortwave CRF values as reported in Wendisch et al. (2019). The broader mode between -60 $\mathrm{W\,m^{-2}}$ and -20 $\mathrm{W\,m^{-2}}$ characterizes the cloudy mode as a function of the prevailing surface albedo and LWP. Applying the estimated cloud-free albedo (red histogram in Fig. 10a), shifts the shortwave CRF in Fig. 10b of the cloudy mode to more negative values, indicating a stronger cooling effect. The non-linearity in the functional dependence of surface albedo and LWP spreads the frequency distribution of corrected CRF, while the mode for cloud-free conditions is not affected.

In total the shortwave CRF shows on average a weak cooling effect of -32 $\mathrm{W\,m^{-2}}$ using the observed albedo values under

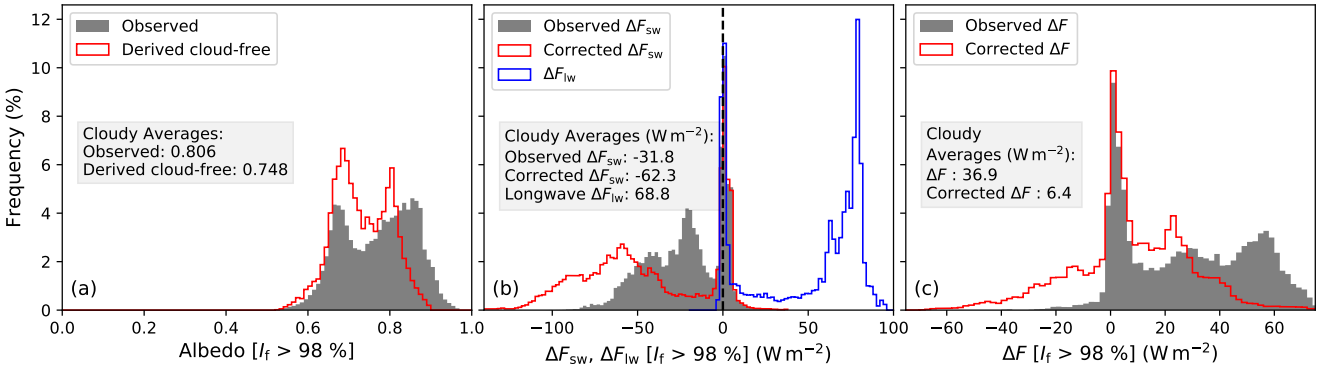

Figure 10. (a) Frequency distribution of the observed (gray) and cloud-free estimated (red) surface albedo for all ACLOUD measurements obtained over homogeneous sea ice ($I_f > 98\,\%$). (b) Terrestrial (blue) and shortwave CRF using the observed albedo (gray) and the shortwave CRF applying the estimated cloud-free albedo (red). (c) The total (shortwave + longwave) CRF calculated with both albedo estimates are shown in panel (c). Average values for cloudy conditions (LWP > 1 g m^{-2}) are given in the embedded text boxes of each panel.

cloudy conditions (LWP > 1 g m^{-2}). Applying the surface albedo for cloud-free conditions almost doubles the shortwave cooling effect to -62 W m^{-2}. These values hold for the ACLOUD observations with an average LWP during cloudy conditions over sea ice of 58 g m^{-2} and a SZA of 61°. In combination with the distribution of the longwave CRF (blue histogram in Fig. 10b), which averages to 69 W m^{-2} in cloudy conditions, the total (shortwave plus longwave) CRF estimate (Fig. 10c) shifts from a significant warming effect of 37 W m^{-2} over sea ice to an in average almost neutral effect (6 W m^{-2}). Also the distribution of the corrected CRF indicates that during the end of the campaign already the cooling effect was dominant (uncorrected mainly positive). Considering that the predominant surface type of the campaign was still sea ice covered by snow, the transition from warming to cooling effect of clouds could already start early in the season, before the formation of melt ponds and the rapid drop in surface albedo, which underlines the potential impact of surface albedo-cloud interactions.

5 Conclusions

To estimate the warming or cooling effect of clouds on the surface REB in the Arctic from observations or models, a precise characterization of the cloud-free state is required. Especially in the transition region between open ocean and closed sea ice (the MIZ), the thermodynamic state of the atmosphere changes on horizontal scales of a few kilometers, which influences the simulated cloud-free radiative field. Also, to obtain reliable estimates of CRF along meridional air mass transports into and out of the Arctic, such as warm air intrusions or cold air outbreaks (Tjernström et al., 2015; Pithan et al., 2018; Tjernström et al., 2019), a high temporal and spatial resolution of thermodynamic profile measurements along the trajectory are required.

Variability in sea ice concentration is closely linked with fluctuations in surface albedo. The derivation of downward irradiances under cloud-free conditions requires an estimate of the effective areal average surface albedo, determining the multiple scattering on large spatial scales. For airborne observations, moving average filters with shapes appropriate of reproducing 3D

radiative transfer need to be applied to obtain values of shortwave CRF adapted to the environment.

The transition between cloudy and cloud-free atmospheric states is accompanied by changes in the radiative transfer, affecting the surface albedo, and the CRF. In the available CRF studies in the Arctic, either observations during cloud-free periods have been used to extrapolate the expected cloud-free surface albedo during cloudy periods, or simply the surface albedo observed in cloudy conditions have been used. As the snow and ice albedo depends on parameters like snow grain size, prevailing SZA, and cloud optical thickness, the available approaches only insufficiently represent the cloud-free albedo in the cloudy Arctic.

Combining spectral snow surface albedo models with atmospheric radiative transfer simulations enables to quantify the impact of two processes related to spectral surface albedo-cloud interactions. The spectral weighting effect of downward irradiance appears to be dominant for snow surfaces and enhances the cooling effect of clouds at the surface. For the second process, a change from mainly direct radiation in the cloud-free state to rather diffuse radiation in the cloudy state, the sign of the modification depends on SZA, cloud optical thickness, and the melting state of sea ice. The changes in shortwave surface albedo with increasing cloud optical thickness are significant and directly impact the shortwave net irradiances, and thus, the estimate of shortwave CRF.

For the ACLOUD campaign, characterized by snow on sea ice in the beginning melting season, the averaged shortwave CRF estimate over homogeneous sea ice of -32 $\mathrm{W\,m^{-2}}$ (cooling) almost doubles to -62 $\mathrm{W\,m^{-2}}$, when surface albedo-cloud interactions are taken into account. The campaign averaged total CRF is shifted from a mainly warming effect of clouds over sea ice to an almost neutral effect, for the ACLOUD observations with relatively small SZA. Hence, the observed albedo trend during the campaign (Fig. 8) induces a transition in CRF from a warming to a cooling already for snow covered surface types, and thus, earlier in the season as reported during SHEBA. In addition, the instantaneous longwave CRF approach might additionally induce an overestimate of the warming effect potentially shifting the total CRF further to cooling. This indicates a possible extension of the period in which clouds cool the surface and highlights the impact of surface albedo-cloud interactions and a required reassessment of the CRF in the Arctic.

Long-term measurements, such as those performed during the SHEBA campaign or currently within the Multidisciplinary drifting Observatory for the Study of Arctic Climate (MOSAiC) expedition (www.mosaic-expedition.org), with an appropriate instrumentation and radiative transfer modelling will be required to quantify these effects and their potential seasonal dependence by continuously estimating the cloud-free albedo in cloudy conditions. The proposed method to estimate the surface albedo in cloud-free conditions using the parameterization from Gardner and Sharp (2010) can be easily applied to common Arctic long-term observations above snow and ice surface types, especially if high quality LWP measurements are available.

Besides observations, global climate models and their estimate of the cloud radiative feedback are based on the impact of clouds on the surface REB, for which the surface albedo is fundamental. For specific surface types, often fixed values of shortwave surface albedo are assigned and parameterized using surface temperature. However, these simplified parameterizations are not appropriate to accurately describe surface albedo-cloud interactions. The use of parameterizations accounting for these effects, such as that of Gardner and Sharp (2010), are necessary and highlight the need for coupled surface atmosphere models including representative surface microphysical properties. The shortwave net irradiances depend not alone on cloud transmissivity and surface albedo, moreover the interaction between both needs to be represented.

Further effort in coupled surface atmosphere radiative transfer modelling with a representation of common surface albedo types like the ones from melt ponds in the Arctic are required to track the seasonal cycle of shortwave CRF. Spectral albedo observations combined with the common broadband devices will help to account for the spectral features in surface albedo and trace changes in SSA. The proposed approach of reproducing the cloud-free albedo can not adequately reflect the diversity of spectral surface albedo types and issues related to the surface albedo-cloud interaction, especially in summer.

Considering the surface albedo-cloud interaction in global climate models and upcoming long-term observations such as MOSAiC will further improve our understanding of CRF and cloud radiative feedback in the Arctic environment and its role for Arctic amplification.

Data availability. The pyranometer and pyrgeometer broadband irradiance and KT-19 nadir brightness temperature from AWI aircraft Polar 5&6 during the May to June 2017 ACLOUD campaign are published on the PANGAEA database (Stapf et al., 2019). The retrieved CRF, LWP equivalent and cloud-free albedo are made avaiable on PANGAEA. Air temperature, relative humidity and pressure in situ profiles from both aircraft are used from (Hartmann et al., 2019). Polar 5 Dropsondes: (Ehrlich et al., 2019a). Calibrated fisheye camera images: (Jäkel and Ehrlich, 2019; Jäkel et al., 2019). Radiosoundings from Polarstern (Schmithüsen, 2017) and Ny-Ålesund (Maturilli, 2017a, b).

Appendix A: Transmissivity-based retrieval of LWP equivalent

The cloud transmissivity is defined by the ratio of measured $F^{\downarrow}_{\mathrm{sw,all}}$ and the simulated cloud-free $F^{\downarrow}_{\mathrm{sw,cf}}$ downward irradiance:

$$\mathcal{T} = \frac{F^{\downarrow}_{\mathrm{sw,all}}}{F^{\downarrow}_{\mathrm{sw,cf}}}. \tag{A1}$$

$\mathcal{T}$ can be converted into cloud optical thickness or LWP, however, it is important to account for the surface albedo dependences due to multiple scattering. The $\mathcal{T}$ for a cloud with the same microphysical properties over snow and ice is higher compared to over open ocean, where the majority of photons will be absorbed by the surface and are not available for new back-scattering events of the upward irradiance in the cloud towards the surface. Taking this dependence into account, the broadband $\mathcal{T}$ is used to derive the cloud optical thickness similar to the approach by Leontyeva and Stamnes (1993).

Lookup tables of $\mathcal{T}$ for a range of surface albedo between 0 and 1 and LWP between 0 and $320\,\mathrm{g\,m^{-2}}$ are simulated for the local solar zenith angle and compared to the values derived from the observations along the flight track. In the simulations, vertically homogeneous pure liquid water clouds are assumed to limit the complexity of the simulations. Therefore, in the following the LWP is referred to an equivalent LWP, because no ice water content is assumed. The cloud is located between $400\,\mathrm{m}$ and $600\,\mathrm{m}$ with a fixed r_{eff} of $8\,\mu\mathrm{m}$, typical for Arctic clouds in this season and region (Mioche et al., 2017). These rather crude assumptions result in uncertainties of the simulated irradiance, which were quantified by Leontyeva and Stamnes (1993) as a function of surface albedo, SZA, r_{eff} and cloud optical thickness.

Similar to the simulations of $F^{\downarrow}_{\mathrm{sw,cf}}$ for heterogeneous surface albedo fields, an effective albedo, which influences the local scattering processes in cloudy conditions needs to be considered in the retrieval simulations of $\mathcal{T}$ (Pirazzini and Raisanen,

2008).

The diversity of potential 3D effects induced by surface and cloud heterogeneities in the MIZ omit a specific solution for the smoothing problem of the areal averaged effective albedo and can only partially be depicted by radiative transfer modelling. To make the retrieval applicable to ACLOUD measurements and reduce the uncertainties induced by horizontal photon transport, a commonly observed cloud/surface scene, with a cloud base height of 200 m and leads with different sizes, are simulated using 3D radiative transfer (not shown here). The estimated kernel k is based on a Cauchy distribution:

$$k(x,\mu,\gamma) = \left(\pi \cdot \gamma \cdot \left[1 + \left(\frac{x-\mu}{\gamma}\right)^2\right]\right)^{-1}, \tag{A2}$$

with γ of 400 m, the median μ and a scale x of 10 km. The horizontal extent is, as expected, smaller compared to the cloud-free kernel introduced in Fig. 3b, due to the low cloud base height limiting the free photon path length. Applied to the theoretical observed albedo the simulated 1D irradiance adequately reproduces the results obtained from the 3D output, and thus, reduces for these cloud/surface scenes the uncertainties of the retrieved LWP considerably.

Nevertheless, multiple scattering, changes in cloud base height (Pirazzini and Raisanen, 2008) and 3D radiative effects due to inhomogeneous cloud/surface scenes, might induce large uncertainties in this retrieval. However, the observed I_f statistics indicate that the majority of ACLOUD flights were conducted over a rather homogeneous surface, where the discussed issue is minor important. The sensitivity of the retrieval is in general higher over open water compared to over ice, since changes in $F_\mathrm{sw}^{\downarrow}$ with increasing LWP are more pronounced. The relative uncertainty range of this retrieval for homogeneous clouds and surface can be expected between 15 % and 35 % over open ocean and sea ice respectively.

The conversion from LWP to optical thickness (τ), as required for the parameterization by Gardner and Sharp (2010), is applied by,

$$\tau = \frac{9}{5} \cdot \frac{\mathrm{LWP}}{\varrho_\mathrm{w} \cdot r_\mathrm{eff}}, \tag{A3}$$

with the density of liquid water ϱ_w and the simulated r_eff.

Author contributions. All authors contributed to the editing of the manuscript and to the discussion of the results. JS drafted the manuscript and initialized the study. JS processed the radiation data, merged the data sets and performed the radiative transfer simulations. EJ contributed to the radiative transfer simulations and their interpretation. MW, AE and CL designed the experimental basis of this study.

Competing interests. The authors declare that they have no conflict of interest.

Acknowledgements. We gratefully acknowledge the funding by the Deutsche Forschungsgemeinschaft (DFG, German Research Foundation) – Project Number 268020496 – TRR 172, within the Transregional Collaborative Research Center "ArctiC Amplification: Climate Relevant

Atmospheric and SurfaCe Processes, and Feedback Mechanisms (AC)³". The authors are grateful to AWI for providing and operating the two aircraft during the ACLOUD campaign. We thank the crews of Polar 5 and Polar 6, the technicians of the aircraft for excellent technical and logistical support. The generous funding of the flight hours for ACLOUD by AWI is greatly appreciated. Observations in Fig. 8 were made by the SHEBA Atmospheric Surface Flux Group, Ed Andreas, Chris Fairall, Peter Guest, and Ola Persson.

References

Anderson, G., Clough, S., Kneizys, F., Chetwynd, J., and Shettle, E.: AFGL Atmospheric Constituent Profiles (0–120 km), Tech. Rep. AFGL-TR-86-0110, AFGL (OPI), Hanscom AFB, MA 01736, 1986.

Benner, T. C., Curry, J. A., and Pinto, J. O.: Radiative transfer in the summertime Arctic, J. Geophys. Res., 106, 15.173–15.183, 2001.

Cohen, J., Screen, J. A., Furtado, J. C., Barlow, M., Whittleston, D., Coumou, D., Francis, J., Dethloff, K., Entekhabi, D., Overland, J., and Jones, J.: Recent Arctic amplification and extreme mid-latitude weather, Nat. Geosci., 7, 627–637, https://doi.org/10.1038/NGEO2234, 2014.

Cox, C. J., Walden, V. P., Rowe, P. M., and Shupe, M. D.: Humidity trends imply increased sensitivity to clouds in a warming Arctic, Nat. Commun., 6, 10 117, https://doi.org/10.1038/ncomms10117, 2015.

Cox, C. J., Uttal, T., Long, C. N., Shupe, M. D., Stone, R. S., and Starkweather, S.: The Role of Springtime Arctic Clouds in Determining Autumn Sea Ice Extent, J. Climate, 29, 6581–6596, https://doi.org/10.1175/JCLI-D-16-0136.1, 2016.

Dong, X. Q., Xi, B. K., and Minnis, P.: A climatology of midlatitude continental clouds from the ARM SGP central facility. Part II: Cloud fraction and surface radiative forcing, J. Climate, 19, 1765–1783, 2006.

Dong, X. Q., Xi, B. K., Crosby, K., Long, C. N., Stone, R. S., and Shupe, M. D.: A 10 year climatology of Arctic cloud fraction and radiative forcing at Barrow, Alaska RID F-8754-2011, J. Geophys. Res., 115, D17 212, https://doi.org/10.1029/2009JD013489, 2010.

Ehrlich, A., Stapf, J., Lüpkes, C., Mech, M., Crewell, S., and Wendisch, M.: Meteorological measurements by dropsondes released from POLAR 5 during ACLOUD 2017, PANGAEA, https://doi.org/10.1594/PANGAEA.900204, 2019a.

Ehrlich, A., Wendisch, M., Lüpkes, C., Buschmann, M., Bozem, H., Chechin, D., Clemen, H.-C., Dupuy, R., Eppers, O., Hartmann, J., Herber, A., Jäkel, E., Järvinen, E., Jourdan, O., Kästner, U., Kliesch, L.-L., Köllner, F., Mech, M., Mertes, S., Neuber, R., Ruiz-Donoso, E., Schnaiter, M., Schneider, J., Stapf, J., and Zanatta, M.: A comprehensive in situ and remote sensing data set from the Arctic CLoud Observations Using airborne measurements during polar Day (ACLOUD) campaign., Earth Syst. Sci. Data Discuss., https://doi.org/10.5194/essd-2019-96, in review, 2019b.

Emde, C., Buras-Schnell, R., Kylling, A., Mayer, B., Gasteiger, J., Hamann, U., Kylling, J., Richter, B., Pause, C., Dowling, T., and Bugliaro, L.: The libRadtran software package for radiative transfer calculations (version 2.0.1), Geosci. Model Dev., 9, 1647–1672, https://doi.org/10.5194/gmd-9-1647-2016, 2016.

Gardner, A. S. and Sharp, M. J.: A review of snow and ice albedo and the development of a new physically based broadband albedo parameterization, J. Geophys. Res., 115, F01 009, https://doi.org/10.1029/2009JF001444, 2010.

Gasteiger, J., Emde, C., Mayer, B., Buras, R., Buehler, S. A., and Lemke, O.: Representative wavelengths absorption parameterization applied to satellite channels and spectral bands, J. Quant. Spectrosc. Ra., 148, 99–115, https://doi.org/10.1016/j.jqsrt.2014.06.024, 2014.

Gillett, N. P., Stone, D. A., Stott, P. A., Nozawa, T., Karpechko, A. Y., Hegerl, G. C., Wehner, M. F., and Jones, P. D.: Attribution of polar warming to human influence, Nat. Geosci., 1, 750–754, https://doi.org/10.1038/ngeo338, 2008.

Goosse, H., Kay, J. E., Armour, K. C., Bodas-Salcedo, A., Chepfer, H., Docquier, D., Jonko, A., Kushner, P. J., Lecomte, O., Massonnet, F., Park, H. S., Pithan, F., Svensson, G., and Vancoppenolle, M.: Quantifying climate feedbacks in polar regions, Nat. Commun., 9, 1919, https://doi.org/10.1038/s41467-018-04173-0, 2018.

Grenfell, T. C. and Perovich, D. K.: Incident spectral irradiance in the Arctic Basin during the summer and fall, J. Geophys. Res., 113, D12 117, https://doi.org/10.1029/2007JD009418, 2008.

Hartmann, J., Lüpkes, C., and Chechin, D.: High resolution aircraft measurements of wind and temperature during the ACLOUD campaign in 2017, PANGAEA, https://doi.pangaea.de/10.1594/PANGAEA.900880, 2019.

Hori, M., Aoki, T., Tanikawa, T., Motoyoshi, H., Hachikubo, A., Sugiura, K., Yasunari, T. J., Eide, H., Storvold, R., Nakajima, Y., and Takahashi, F.: In-situ measured spectral directional emissivity of snow and ice in the 8-14 mu m atmospheric window, Remote Sens. Environ., 100, 486–502, https://doi.org/10.1016/j.rse.2005.11.001, 2006.

Intrieri, J. M., Fairall, C. W., Shupe, M. D., Persson, P. O. G., Andreas, E. L., Guest, P. S., and Moritz, R. E.: An annual cycle of Arctic surface cloud forcing at SHEBA, J. Geophys. Res., 107, 8039, 2002.

Iwabuchi, H.: Efficient Monte Carlo methods for radiative transfer modeling, J. Atmos. Sci., 63, 2324–2339, 2006.

Iwabuchi, H. and Kobayashi, H.: Modeling of radiative transfer in cloudy atmospheres and plant canopies using Monte Carlo methods, Tech. Rep., 8, 199 pp., 2008.

Jäkel, E. and Ehrlich, A.: Radiance fields of clouds and the Arctic surface measured by a digital camera during ACLOUD 2017, PANGAEA, https://doi.pangaea.de/10.1594/PANGAEA.901024, 2019.

Jäkel, E., Stapf, J., Wendisch, M., Nicolaus, M., Dorn, W., and Rinke, A.: Validation of the sea ice surface albedo scheme of the regional climate model HIRHAM-NAOSIM using aircraft measurements during the ACLOUD/PASCAL campaigns, Cryosphere, 13, 1695–1708, https://doi.org/10.5194/tc-13-1695-2019, 2019.

Jeffries, M. O., Overland, J. E., and Perovich, D. K.: The Arctic shifts to a new normal, Phys. Today, 66, 35–40, 2013.

Kato, S., Ackerman, T., Mather, J., and Clothiaux, E.: The k-distribution method and correlated-k approximation for a shortwave radiative transfer model, J. Quant. Spectrosc. Ra., 62, 109–121, 1999.

Knudsen, E. M., Heinold, B., Dahlke, S., Bozem, H., Crewell, S., Gorodetskaya, I. V., Heygster, G., Kunkel, D., Maturilli, M., Mech, M., Viceto, C., Rinke, A., Schmithüsen, H., Ehrlich, A., Macke, A., Lüpkes, C., and Wendisch, M.: Meteorological conditions during the ACLOUD/PASCAL field campaign near Svalbard in early summer 2017, Atmos. Chem. Phys., 18, 17 995–18 022, https://doi.org/10.5194/acp-18-17995-2018, 2018.

Kreuter, A., Buras, R., Mayer, B., Webb, A., Kift, R., Bais, A., Kouremeti, N., and Blumthaler, M.: Solar irradiance in the heterogeneous albedo environment of the Arctic coast: measurements and a 3-D model study, Atmos. Chem. Phys., 14, 5989–6002, https://doi.org/10.5194/acp-14-5989-2014, 2014.

Lampert, A., Maturilli, M., Ritter, C., Hoffmann, A., Stock, M., Herber, A., Birnbaum, G., Neuber, R., Dethloff, K., Orgis, T., Stone, R., Brauner, R., Kassbohrer, J., Haas, C., Makshtas, A., Sokolov, V., and Liu, P.: The spring-time boundary layer in the central Arctic observed during PAMARCMiP 2009, Atmosphere-Basel, 3, 320–351, https://doi.org/10.3390/atmos3030320, 2012.

Leontyeva, E. and Stamnes, K.: Estimation of cloud optical thickness from ground-based measurements of incoming solar radiation in the Arctic, J. Climate, 7, 566–578, 1993.

Libois, Q., Picard, G., France, J. L., Arnaud, L., Dumont, M., Carmagnola, C. M., and King, M. D.: Influence of grain shape on light penetration in snow, Cryosphere, 7, 1803–1818, https://doi.org/10.5194/tc-7-1803-2013, 2013.

Long, C. and Ackerman, T.: Identification of clear skies from broadband pyranometer measurements and calculation of downwelling shortwave cloud effects, J. Geophys. Res., 105, 15 609–15 626, 2000.

Long, C. N.: On the estimation of clear-sky upwelling SW and LW, Fifteenth ARM Science Team Meeting Proceedings, Daytona Beach, Florida, March 14–18, 2005.

Long, C. N. and Turner, D. D.: A method for continuous estimation of clear-sky downwelling longwave radiative flux developed using ARM surface measurements, J. Geophys. Res., 113, D18 206, https://doi.org/10.1029/2008JD009936, 2008.

Maturilli, M.: High resolution radiosonde measurements from station Ny-Ålesund (2017-05), PANGAEA, https://doi.org/10.1594/PANGAEA.879820, 2017a.

Maturilli, M.: High resolution radiosonde measurements from station Ny-Ålesund (2017-06), PANGAEA, https://doi.org/10.1594/PANGAEA.879822, 2017b.

Miller, N. B., Shupe, M. D., Cox, C. J., Walden, V. P., Turner, D. D., and Steffen, K.: Cloud Radiative Forcing at Summit, Greenland, J. Climate, 28, 6267–6280, https://doi.org/10.1175/JCLI-D-15-0076.1, 2015.

Miller, N. B., Shupe, M. D., Lenaerts, J. T. M., Kay, J. E., de Boer, G., and Bennartz, R.: Process-Based Model Evaluation Using Surface Energy Budget Observations in Central Greenland, J. Geophys. Res., 123, 4777–4796, https://doi.org/10.1029/2017JD027377, 2018.

Mioche, G., Jourdan, O., Delanoe, J., Gourbeyre, C., Febvre, G., Dupuy, R., Monier, M., Szczap, F., Schwarzenboeck, A., and Gayet, J. F.: Vertical distribution of microphysical properties of Arctic springtime low-level mixed-phase clouds over the Greenland and Norwegian seas, Atmos. Chem. Phys., 17, 12 845–12 869, https://doi.org/10.5194/acp-17-12845-2017, 2017.

Overland, J. E., Wood, K. R., and Wang, M.: Warm Arctic–cold continents: Impacts of the newly open Arctic Sea, Polar Res., 30, 15 787, doi:10.3402/polar.v30i0.15 787, 2011.

Perovich, D. K., Grenfell, T. C., Light, B., and Hobbs, P. V.: Seasonal evolution of the albedo of multiyear Arctic sea ice, J. Geophys. Res., 107, https://doi.org/10.1029/2000JC000438, 8044, 2002.

Pirazzini, R. and Raisanen, P.: A method to account for surface albedo heterogeneity in single-column radiative transfer calculations under overcast conditions, J. Geophys. Res., 113, https://doi.org/10.1029/2008JD009815, 2008.

Pithan, F. and Mauritsen, T.: Arctic amplification dominated by temperature feedbacks in contemporary climate models, Nature, 7, 181–184, https://doi.org/10.1038/ngeo2071, 2014.

Pithan, F., Svensson, G., Caballero, R., Chechin, D., Cronin, T. W., Ekman, A. M. L., Neggers, R., Shupe, M. D., Solomon, A., Tjernstrom, M., and Wendisch, M.: Role of air-mass transformations in exchange between the Arctic and mid-latitudes, Nat. Geosci., 11, 805–812, https://doi.org/10.1038/s41561-018-0234-1, 2018.

Podgorny, I., Lubin, D., and Perovich, D. K.: Monte Carlo Study of UAV-Measurable Albedo over Arctic Sea Ice, J. Atmos. Ocean. Tech., 35, 57–66, https://doi.org/10.1175/JTECH-D-17-0066.1, 2018.

Ramanathan, V., Cess, R, D., Harrison, E. F., Minnis, P., Barkstrom, B. R., Ahmad, E., and Hartmann, D.: Cloud-radiative forcing and climate: Results from the Earth Radiation Biudget Experiment, Science, 243, 57–63, 1989.

Randles, C. A., Kinne, S., Myhre, G., Schulz, M., Stier, P., Fischer, J., Doppler, L., Highwood, E., Ryder, C., Harris, B., Huttunen, J., Ma, Y., Pinker, R. T., Mayer, B., Neubauer, D., Hitzenberger, R., Oreopoulos, L., Lee, D., Pitari, G., Di Genova, G., Quaas, J., Rose, F. G., Kato, S., Rumbold, S. T., Vardavas, I., Hatzianastassiou, N., Matsoukas, C., Yu, H., Zhang, F., Zhang, H., and Lu, P.: Intercomparison of shortwave radiative transfer schemes in global aerosol modeling: results from the AeroCom Radiative Transfer Experiment, Atmos. Chem. Phys., 13, 2347–2379, https://doi.org/10.5194/acp-13-2347-2013, 2013.

Ricchiazzi, P. and Gautier, C.: Investigation of the effect of surface heterogeneity and topography on the radiation environment of Palmer Station, Antarctica, with a hybrid 3-D radiative transfer model, J. Geophys. Res., 103, 6161–6178, 1998.

Schmithüsen, H.: Upper air soundings during POLARSTERN cruise PS106.1 (ARK-XXXI/1.1), PANGAEA, https://doi.org/10.1594/PANGAEA.882736, 2017.

Screens, J. A. and Simmonds, I.: The central role of diminishing sea ice in recent Arctic temperature amplification, Nature, 464, 1334–1337, 2010.

Sedlar, J., Tjernstrom, M., Mauritsen, T., Shupe, M. D., Brooks, I. M., Persson, P. O. G., Birch, C. E., Leck, C., Sirevaag, A., and Nicolaus, M.: A transitioning Arctic surface energy budget: the impacts of solar zenith angle, surface albedo and cloud radiative forcing RID F-8754-2011, Climate Dyn., 37, 1643–1660, https://doi.org/10.1007/s00382-010-0937-5, 2011.

Serreze, M. C. and Barry, R. G.: Processes and impacts of Arctic amplification: A research synthesis, Global Planet. Change, 77, 85–96,doi:10.1016/j.gloplacha.2011.03.004, 2011.

Shupe, M. D. and Intrieri, J. M.: Cloud radiative forcing of the Arctic surface: The influence of cloud properties, surface albedo, and solar zenith angle, J. Climate, 17, 616–628, 2004.

Shupe, M. D., Walden, V. P., Eloranta, E., Uttal, T., Campbell, J. R., Starkweather, S. M., and Shiobara, M.: Clouds at Arctic Atmospheric Observatories. Part I: Occurrence and Macrophysical Properties, J. Appl. Meteorol., 50, 626–644, https://doi.org/10.1175/2010JAMC2467.1, 2011.

Spreen, G., Kaleschke, L., and Heygster, G.: Sea ice remote sensing using AMSR-E 89-GHz channels, J. Geophys. Res., 113, C02S03, https://doi.org/10.1029/2005JC003384, 2008.

Stamnes, K., Tsay, S., Wiscombe, W., and Jayaweera, K.: A numerically stable algorithm for discrete-ordinate-method radiative transfer in multiple scattering and emitting layered media, Appl. Opt., 27, 2502–2509, 1988.

Stapf, J., Ehrlich, A., Jäkel, E., and Wendisch, M.: Aircraft measurements of broadband irradiance during the ACLOUD campaign in 2017, PANGAEA, https://doi.org/10.1594/PANGAEA.900442, 2019.

Stramler, K., Del Genio, A. D., and Rossow, W. B.: Synoptically Driven Arctic Winter States, J. Climate, 24, 1747–1762, https://doi.org/10.1175/2010JCLI3817.1, 2011.

Stroeve, J. C., Serreze, M. C., Holland, M. M., Kay, J. E., Maslanik, J., and Barrett, A. P.: The Arctic's rapidly shrinking sea ice cover: A research synthesis, Climatic Change, 110, 1005–1027, doi:10.1007/s10 584–011–0101–1, 2012.

Tjernström, M. and Graversen, R. G.: The vertical structure of the lower Arctic troposphere analysed from observations and the ERA-40 reanalysis, Quart. J. Roy. Meteor. Soc., 135, 431–443, https://doi.org/10.1002/qj.380, 2009.

Tjernström, M., Shupe, M. D., Brooks, I. M., Persson, P. O. G., Prytherch, J., Salisbury, D. J., Sedlar, J., Achtert, P., Brooks, B. J., Johnston, P. E., Sotiropoulou, G., and Wolfe, D.: Warm-air advection, air mass transformation and fog causes rapid ice melt, Geophys. Res. Lett., 42, 5594–5602, https://doi.org/10.1002/2015GL064373, 2015.

Tjernström, M., Shupe, M. D., Brooks, I. M., Achtert, P., Prytherch, J., and Sedlar, J.: Arctic Summer Airmass Transformation, Surface Inversions, and the Surface Energy Budget, J. Climate, 32, 769–789, https://doi.org/10.1175/JCLI-D-18-0216.1, 2019.

Uttal, T., Curry, J. A., McPhee, M. G., Perovich, D. K., Moritz, R. E., Maslanik, J. A., Guest, P. S., Stern, H. L., Moore, J. A., Turenne, R., Heiberg, A., Serreze, M. C., Wylie, D. P., Persson, O. G., Paulson, C. A., Halle, C., Morison, J. H., Wheeler, P. A., Makshtas, A., Welch, H., Shupe, M. D., Intrieri, J. M., Stamnes, K., Lindsey, R. W., Pinkel, R., Pegau, W. S., Stanton, T. P., and Grenfeld, T. C.: Surface heat budget of the Arctic Ocean, B. Am. Meteorol. Soc., 83, 255–275, https://doi.org/10.1175/1520-0477(2002)083<0255:SHBOTA>2.3.CO;2, 2002.

Walsh, J. E. and Chapman, W. L.: Arctic cloud-radiation-temperature associations in observational data and atmospheric reanalyses, J. Climate, 11, 3030–3045, https://doi.org/10.1175/1520-0442(1998)011<3030:ACRTAI>2.0.CO;2, 1998.

Wang, W. S., Zender, C. S., and van As, D.: Temporal Characteristics of Cloud Radiative Effects on the Greenland Ice Sheet: Discoveries From Multiyear Automatic Weather Station Measurements, J. Geophys. Res., 123, 11 348–11 361, https://doi.org/10.1029/2018JD028540, 2018.

Warren, S.: Optical Properties of Snow, Rev. Geophys. Space Phys., 20, 67–89, 1982.

Weihs, P., Lenoble, J., Blumthaler, M., Martin, T., Seckmeyer, G., Philipona, R., de la Casiniere, A., Sergent, C., Gröbner, J., Cabot, T., Masserot, D., Pichler, T., Pougatch, E., Rengarajan, G., Schmucki, D., and Simic, S.: Modeling the effect of an inhomogeneous surface albedo on incident UV radiation in mountaineous terrain: determination of an effective surface albedo, Geophys. Res. Lett., 28, 3111–3114, 2001.

Wendisch, M., Pilewskie, P., Jäkel, E., Schmidt, S., Pommier, J., Howard, S., Jonsson, H. H., Guan, H., Schröder, M., and Mayer, B.: Airborne measurements of areal spectral surface albedo over different sea and land surfaces, J. Geophys. Res., 109, Art. No. D08 203, https://doi.org/doi:10.1029/2003JD004392, 2004.

Wendisch, M., Brückner, M., Burrows, J. P., Crewell, S., Dethloff, K., Ebell, K., Lüpkes, C., Macke, A., Notholt, J., Quaas, J., Rinke, A., and Tegen, I.: Understanding causes and effects of rapid warming in the Arctic, Eos, 98, https://doi.org/10.1029/2017EO064803, 2017.

Wendisch, M., Macke, A., Ehrlich, A., Lüpkes, C., Mech, M., Chechin, D., Barrientos, C., Bozem, H., Brückner, M., Clemen, H.-C., Crewell, S., Donth, T., Dupuy, R., Ebell, K., Egerer, U., Engelmann, R., Engler, C., Eppers, O., Gehrmann, M., Gong, X., Gottschalk, M., Gourbeyre, C., Griesche, H., Hartmann, J., Hartmann, M., Herber, A., Herrmann, H., Heygster, G., Hoor, P., Jafariserajehlou, S., Jäkel, E., Järvinen, E., Jourdan, O., Kästner, U., Kecorius, S., Knudsen, E. M., Köllner, F., Kretzschmar, J., Lelli, L., Leroy, D., Maturilli, M., Mei, L., Mertes, S., Mioche, G., Neuber, R., Nicolaus, M., Nomokonova, T., Notholt, J., Palm, M., van Pinxteren, M., Quaas, J., Richter, P., Ruiz-Donoso, E., Schäfer, M., Schmieder, K., Schnaiter, M., Schneider, J., Schwarzenböck, A., Seifert, P., Shupe, M. D., Siebert, H., Spreen, G., Stapf, J., Stratmann, F., Vogl, T., Welti, A., Wex, H., Wiedensohler, A., Zanatta, M., and Zeppenfeld, S.: The Arctic cloud puzzle: using ACLOUD/PASCAL multi-platform observations to unravel the role of clouds and aerosol particles in Arctic amplification, B. Am. Meteorol. Soc., 100 (5), 841–871, https://doi.org/10.1175/BAMS-D-18-0072.1, 2019.